

Cronfa - Swansea University Open Access Repository

This is an author produced version of a paper published in:

International Journal of Plasticity

Cronfa URL for this paper:

<http://cronfa.swan.ac.uk/Record/cronfa48800>

Paper:

Birosca, S., Liu, G., Ding, R., Jiang, J., Simm, T., Deen, C. & Whittaker, M. (2019). The dislocation behaviour and GND development in a nickel based superalloy during creep. *International Journal of Plasticity*

<http://dx.doi.org/10.1016/j.ijplas.2019.02.015>

This item is brought to you by Swansea University. Any person downloading material is agreeing to abide by the terms of the repository licence. Copies of full text items may be used or reproduced in any format or medium, without prior permission for personal research or study, educational or non-commercial purposes only. The copyright for any work remains with the original author unless otherwise specified. The full-text must not be sold in any format or medium without the formal permission of the copyright holder.

Permission for multiple reproductions should be obtained from the original author.

Authors are personally responsible for adhering to copyright and publisher restrictions when uploading content to the repository.

<http://www.swansea.ac.uk/library/researchsupport/ris-support/>

The Dislocation Behaviour and GND Development in a Nickel Based Superalloy during Creep

Soran Biroscă¹, Gang Liu¹, Rengen Ding², Jun Jiang³, Thomas Simm¹, Chris Deen⁴, Mark Whittaker¹

¹ Institute of Structural Materials, College of Engineering, Swansea University, Bay Campus,
Swansea SA1 8EN, UK.

² School of Metallurgy and Materials, University of Birmingham, Birmingham B15 2TT, UK.

³ Department of Mechanical Engineering, Faculty of Engineering, South Kensington Campus,
Imperial College London, London SW7 2AZ, UK

⁴ Rolls-Royce plc, PO Box 31, Derby, DE24 8BJ, UK.

Abstract

In the current study, dislocation activity and storage during creep deformation in a nickel based superalloy (Waspaloy) were investigated, focussing on the storage of geometrically necessary (GND) and statistically stored (SSD) dislocations. Two methods of GND density calculation were used, namely, EBSD Hough Transformation and HR-EBSD Cross Correlation based methods. The storage of dislocations, including SSDs, was investigated by means of TEM imaging. Here, the concept of GND accumulation in soft and hard grains and the effect of neighbouring grain orientation on total dislocation density was examined. Furthermore, the influence of applied stress (below and above the yield stress of Waspaloy) during creep on deformation micro-mechanism and dislocation density was studied. It was demonstrated that soft grains provided pure shear conditions on at least two octahedral (111) slip systems for easy dislocation movement. This allowed dislocations to reach the grain boundary without significant geometrically necessary dislocation accumulation in the centre of the grain. Hence, the majority of the soft grains appeared to have minimum GND density in the centre of the grain with high GND accumulation in the vicinity of the grain boundaries. However, the values

and width of accumulated GND depended on the surrounding grain orientations. Furthermore, it was shown that the hard grains were not favourably oriented for octahedral slip system activation leading to a grain rotation in order to activate any of the available slip systems. Eventually, (i) the hard grain resistance to deformation and (ii) neighbouring grain resistance for the hard grain reorientation caused high GND density on a number of octahedral (111) slip systems. The results also showed that during creep below the yield stress of Waspaloy (500 MPa/700°C), the GND accumulation was relatively low due to the insufficient macroscopic stress level. However, the regions near grain boundaries showed high GND density. At 800 MPa/700°C (above yield at this temperature), in addition to the movement of pre-existing dislocations (SSD and GND) at a higher mobility rate, large numbers of dislocations were generated and moved toward the grain boundaries. This resulted in a much higher GND density but narrower width of high intensity GNDs near the grain boundaries. It is concluded that although GND measurement by means of EBSD can provide great insight into dislocation accumulation and its behaviour, it is critical to consider SSD type which also contributes to the strain hardening of the material.

Keywords: EBSD, Dislocation, GND, Nickel, Superalloy, Creep, TKD.

1. Introduction

Waspaloy, a registered trademark of Pratt & Whitney Aircraft, is a precipitation hardened nickel based superalloy which was developed from the Nimonic series of alloys. Waspaloy has considerable strength and corrosion resistance at temperatures up to 870°C [Whittaker et al., 2017]. As in other nickel based superalloys, Waspaloy is strengthened by a fine dispersion of γ' particles, $\text{Ni}_3(\text{Al},\text{Ti})$, which has an ordered $\text{L}1_2$ structure and precipitates coherently in the nickel-rich FCC (γ) matrix. Waspaloy, a wrought superalloy, is a promising candidate material for use in superheater and reheater tubes as a substitute for 9-12% Cr steels in power plants [Viswanathan and Bakker 2001] in addition to its wide applications in gas turbine discs [Yao et al., 2013 and Penkall et al., 2003]. However,

Waspaloy is subjected to creep deformation at relatively high temperatures in jet engine applications. Moreover, for large scale power plant applications creep damage is widely considered to be the most critical damage mechanism, and often determines the operational conditions. Creep deformation in Waspaloy is therefore of great industrial and academic research interest. Moreover, a better understanding of the creep deformation mechanisms can guide towards improved mechanical properties, which can be achieved through the optimisation of thermomechanical processing routes.

In terms of developing relationships that adequately describe creep behaviour, particularly extrapolation towards long lives, it is recognised that power law based techniques which are not linked to micro-mechanical behaviour are also at risk of failing to capture behavioural changes which show marked changes in material creep life [Whittaker et al., 2017]. The opportunity to design optimised creep resistant alloys, however is dependent on understanding the manifestation of creep damage within the microstructure of materials and particularly the localisation of creep strain in the vicinity of grain boundaries. Recent applications of the Wilshire equations have offered an alternative interpretation to traditional power law type equations where a transition between dislocation and diffusional creep is assumed based on the exponent in Norton's law. Specifically, the approach focusses on the dominance of dislocation creep and attempts to reconcile transitions in behaviour with observed micromechanical phenomena such as yield and the onset of overaging in materials. A key element of the Wilshire equations has been the concept of an apparent activation energy for creep which is a function of stress. The ability to 'region split' based on this parameter has allowed these regions to be linked to specific micromechanical behaviour. Previous research has linked changes in this activation energy to the localisation of dislocation activity in grain boundary zones as proposed by Whittaker and Wilshire, 2013, or the change from interaction with precipitates to a forest hardening mechanism detailed by Whittaker et al., 2017. It is clear that a detailed understanding of strain distribution within the microstructure is critical in the description of creep behaviour and its application to constitutive equations.

For the past 50 years, numerous theoretical, experimental and computer simulation studies have been conducted on creep deformation of nickel based superalloys. However, most of the studies in the literature have been based on dislocation based theories to understand the development, generation, movement, accumulation and mobility of dislocations during loading. Yet, due to the complexity of superalloy systems, dislocation plasticity theory cannot suitably describe creep deformation mechanisms. This is partly due to the limitations of micro- and nano-analytical tools to depict the exact behaviour of dislocations during high temperature static loading. For instance, Transmission Electron Microscopy (TEM) can image all types of dislocations including Geometrically Necessary (GND) and Statistically Stored (SSD) dislocations without an appropriate differentiating method in TEM to recognise both types [Rae and Reed 2007, Pyczak et al., 2005, Wosik et al., 2001]. Electron Backscatter Diffraction (EBSD), however, can calculate GND type, but cannot recognise SSD type [Pantleon 2005, 2008, Kerr 2013]. Moreover, unlike TEM, EBSD diffraction-based tools cannot visualize any type of dislocations due to current EBSD spatial and angular resolutions, thus the GND can only be calculated from EBSD misorientation data. This is related to the fact that GND measurement is totally dependent on EBSD misorientation data that has a geometrical effect on heterogenous plastic strain distributions. Therefore, in the current study the dislocation characteristics were investigated by means of EBSD as well as TEM in order to obtain a comprehensive understanding of dislocation behaviour during creep deformation. A significant difficulty in undertaking this is that the imaging based dislocation observation in TEM is a totally different concept from non-imaging misorientation based dislocation measurement in EBSD. This is more related to the nature and types of dislocation storage phenomena. In general, dislocations are stored because they accumulate by trapping each other in a random way, i.e., SSDs, or they are required for compatible deformation of various parts of the material, i.e., GNDs [Gao et al., 1999, Gao and Huang, 2003, Guo et al., 2014]. Therefore, SSD do not contribute to the lattice curvature, i.e., misorientation values. Another difficulty in capturing the effect on SSD type using diffraction based EBSD data is that a SSD dislocation is assumed to move and glide to relax the stress without leaving a geometrical plastic effect in the material [Gao and Huang 2003]. However, GNDs align themselves to

accommodate the lattice curvature which clearly can have a significant geometric plastic effect [Arsenlis and Park 1999]. Therefore, in the current investigation both TEM and EBSD tools for dislocation behavior observations were utilised on the same Area of Interest (AOI) of the crept specimens.

The dislocation accumulation in the vicinity of grain boundaries and interfaces in polycrystalline materials has been a debated topic for a long time [Alexandreanu 2003, Ashby 1970, Gourges 2002, Jiang et al, 2013). This topic is thoroughly investigated here as the authors of this study believe that the location of “highest” dislocation density within the grains or near the grain boundary gives a significant insight of heterogenous plastic deformation mechanism and may influence the value of the activation energy used within the Wilshire equation approach. GND accumulation near the interfaces is reported in many studies including [Ashby 1970, Sun et al., 2000, Wright et al., 1988, Pantleon et al., 2008, Jiang et al., 2012] and some have assumed GNDs to be stored at the interface [Kubin and Mortensen 2003]. The dislocation accumulation within individual grains away from grain boundaries was also investigated by EBSD. For instance, Field et al., 2005, reported that under certain conditions of plastic deformation of polycrystalline materials, individual grains can be subdivided into crystallites and rotate independently to accommodate the imposed plastic strain. They attributed this “grain fragmentation” to the number and selection of simultaneously acting slip system differences between “neighboring volume elements” within a grain, claiming that this would eventually lead to lattice rotation variations between neighboring “elements” when the material is strained. Di Gioacchino and Joao, 2015 considered the localised lattice rotation within an individual grain as a “deformation domain” and claimed that it was largely affected by slip band directions and strain incompatibilities between the grains. Sun et al., 2000, also reported that lattice curvature was observed near interfaces. They claimed that the GND accumulations at or near grain boundaries was dependent on the strain level imposed on the material. They also showed through experimental observation that interfaces can resist the motion of lattice dislocations, or absorb or emit them depending upon the structure of the interface and local stress states. Furthermore, Ashby 1970, and

recently by Zhu et al., 2018, demonstrated that at small strain condition, the dislocation density and hence work hardening is controlled by GNDs. At large strain condition however, work hardening at the later stage of plastic deformation is mainly controlled by SSDs. They also stated that GNDs dominate the total density at small strains but can be swamped by the SSDs at larger strains. In the current investigation, the validity of these theories and postulations is assessed using TEM imaging based technique to depict both SSD and GND types and diffraction based EBSD tool for GND measurements.

2. Experimental Procedures

2.1 Materials Used and Creep Testing Conditions

The nickel based superalloy, Waspaloy was used in this study, which was supplied by Rolls-Royce plc. The chemical composition of Waspaloy is shown in Table 1. The samples of Waspaloy used for testing were from a forged disc, which had a typical heat treatment of 995-1040°C for 4 hours (h), air cooled (AC), followed by a stabilisation period at 845°C for 4 h / AC, and then aged at 760°C / 16 h / AC. The original materials were characterised prior to creep testing by means of SEM, EDS and EBSD. The creep tests were conducted on Waspaloy at 500 MPa / 700°C and 800 MPa / 700°C, below and above the yield stress (approximately 730 MPa at 700°C) of Waspaloy, respectively. The creep tests were completed in air using a Mayes constant stress creep machine with a loading lever ratio of 15:1 for stresses above 10 MPa (discounting the onset of tertiary failure and necking). Specimen strains were monitored using extensometers incorporating a pair of ASL differential capacitance transducers capable of resolving changes in gauge length to 10 nm. Both creep tests were conducted at 700°C, measured using 2 R type thermocouples, to an accuracy of +/-3°C between thermocouples. All loading, temperature and strain monitoring systems are calibrated annually, in line with BS EN ISO 7500-2 and BS EN ISO 9513.

As mentioned in Section 1, the description of Wilshire equation in terms of minimum creep rate was used rather than the secondary creep rate. This is due the fact that many researchers have questioned the existence of a true steady-state (secondary) creep rate, as the decaying primary stage is immediately offset by the accelerating tertiary phase, resulting only in a minimum, and not a steady state, creep rate [Whittaker et al., 2017]. Thus, the tests conducted in the current study were stopped at the minimum strain rate condition, frequently recalculated during test progression, using the secant method. Following the attainment of the minimum creep rate, specimens were air cooled immediately. For the creep test performed at 500 MPa, the test was interrupted at 21 h (0.25% creep strain), the time associated with the minimum strain rate. The specimens crept at 800 MPa reached the minimum strain rate in 2 h (4.4% creep strain).

2.2 Materials Characterisations

2.2.1 Transmission Electron Microscopy (TEM)

In preparation for TEM analysis, thin discs were cut from within the gauge length of the crept specimen, to an approximate thickness of 0.5 mm, using a high precision cutting wheel. These discs were mounted onto a grinding tool using MWH135 mounting wax. The discs were then progressively ground using grit 800, 1200 and 1500 grade paper to a thickness of 150-200 μm . The spark erosion machine was used to produce 3 mm diameter foils. The resulting 3 mm diameter TEM foils were thinned to a central perforation (hole), using a twin-jet electropolisher (Struers Tenupol III). A polishing solution of 10 vol.% perchloric acid in methanol was used at -25°C and 25 V. All TEM foils were taken from the crept sample loading cross section plane (i.e., perpendicular to the gauge length) so that the Loading Direction (LD) was orthogonal to the plane of the TEM disc (i.e., Normal Direction (ND) as indicated in the presented maps in this study).

2.2.2 Scanning Electron Microscopy (SEM) and Electron Backscatter Diffraction (EBSD)

For SEM characterisation, no further sample preparation was needed, subsequently the Waspaloy TEM foils were directly used for SEM and EBSD characterisations in order to investigate the same areas of interest (AOI). EBSD was used to estimate the influence of plastic strain through misorientation analysis and subsequent GND calculations. Standard EBSD working conditions, *i.e.*, 20 kV acceleration voltage with 15 mm working distance (WD), was used and the orientation data was collected using 100 nm step size in order to determine the orientation spread within individual grains at relatively small length scales. The EBSD obtained data was then analysed using the HKL-Channel 5 analysis packages. The GND and Slip Trace maps were generated from EBSD data using in-house code. The principle of GND and Slip Trace maps calculations is reported in Biroscă et al., 2014, Liu et al., 2018.

The diffraction pattern binning of 4 x 4 was employed and the noise floor was calculated using the method described in [Jiang et al., 2013] and is found to be much less than average GND values. Jiang, et al. 2013, demonstrated that during high resolution EBSD scan the noise floor increased with decreasing step size. However, they also showed that in the deformed materials the average GND density stays relatively constant as the degree of pattern binning is increased from 1 x 1 to 8 x 8 [Jiang et al., 2013], which is the case in this study. In general, using a large step size will reduce the noise level and enable EBSD scanning of larger regions but will result in many GNDs being counted as SSDs and therefore discrimination of key structures, such as dislocation cell walls, will be less clear [Jiang et al., 2013]. A compromise must be made in the step size selection process as the appropriate step size depends on several factors such as the original dislocation density stored in samples, angular resolution and the step size of EBSD maps. When one adjusts these variables, the most important issue is that the measured GND density must be above the noise floor. Thus, in the current study the EBSD orientation data are collected with 100 nm step size in order to determine the orientation spread within individual grains at small length scales. This EBSD step size was chosen to be small enough so as microscopically relevant and large enough to filter out the EBSD noise (averaging the scatter

due to EBSD angular resolution limits). The detailed procedure for selecting the correct EBSD scan step size can be found in [Kerr 2013].

2.2.3 Transmission Kikuchi Diffraction (TKD)

All TKD and EBSD scans were performed using a Jeol JSM-7800F Field Emission Gun Scanning Electron Microscope (FEG-SEM) with Nordlys Nano hardware and AZtec 2.1 software package that acquire TKD, EBSD and Energy Dispersive X-ray Spectroscopy (EDS) data. The same TKD procedure as detailed in Biroscia et al., 2015, was used here. The TEM foil was mounted using a micro-clamp SEM sub-stage which was fixed to a standard 70° tilted EBSD sample holder. At first, the SEM stage was tilted towards the EBSD detector by 20°, resulting in the TEM foils being positioned horizontally. The samples were positioned at a short working distance (typically 5 -8 mm), and the phosphor screen, *i.e.*, EBSD detector, was fully inserted into its standard operating position. The top edge of the EBSD detector's phosphor screen was just below the sample level. The operating voltage used was in the range of 25- 30 kV to optimize the quality of the transmitted Diffraction Patterns (DP), with no image tilt correction applied. An EBSD step size of 50 nm was used for all TKD mappings. Furthermore, the beam current in the range of 4-8 nA was used to enhance the DP quality. However, TEM specimen shadowing was an issue and poor DP quality was produced when the data was collected from a specimen at zero tilt. In the current study tilting the TEM foil by 8-12° was found to optimise the DP quality. Thus, a data collection geometry with TEM foils inclined at 10° above the horizontal axis and facing away from the EBSD hardware such that forward scattered patterns could be recorded on the phosphor screen was used. Routine calibration procedures and indexing optimisation of the obtained DP were performed with the pattern centre situated near the top side of the phosphor screen. The analysis was conducted using a standard HKL-EBSD Channel 5 software package. Minor cleaning to remove the non-indexed points was performed in addition to a careful filtering to reduce noise floor.

2.2.4 High Resolution (HR) EBSD and Cross Correlation Strain Analyses

The principle and methodology of collecting diffraction patterns and cross correlation strain data are reported in Britton and Wilkinson, 2012. HR-EBSD was performed using EBSD data collected on a Quanta FEG-SEM equipped with a Bruker eFlashHR detector operating with 2×2 binning. Cross correlation was utilised to calculate GND density after HR-EBSD scanning. GND analysis of the HR-EBSD data was performed using an L1 based line minimisation determined from lattice curvature data employing the 18 FCC $\{111\} <110>$ FCC slip systems.

2.2.5 GND and Slip Trace Mapping using EBSD Data

The calculations of generated EBSD-GND maps are based on quantification of crystal orientation spread within individual grains that arise due to dislocation accumulation during heterogeneous plastic deformation. Recently, EBSD has become a key tool for studying elastic [Wilkinson 2001] and plastic [El-Dahser et al., 2003, Field et al., 2005, Wilkinson et al., 2006a, Wilkinson et al., 2006b, Kamaya at al., 2006, Demir et al., 2009] strains quantitatively, by measuring the relative deformation gradient and lattice curvature, respectively. From the orientation differences between neighbouring points the lattice curvature and the dislocation density tensor can be derived as the minimal effect of elastic stress can be neglected [Demir et al., 2009, Pantleon 2008, Gao et al., 1999, Needleman and Sevillano, 2003]. The plastic deformation can introduce orientation differences in originally homogenously oriented grains. Any local excess of dislocations of one sign of Burger vector causes an orientation spread. During plastic deformation GNDs accommodate these orientation gradients within individual grains in the materials and represent the minimum necessary density to maintain lattice continuity [Field at al., 2005, Cater et al., 2014, Calcagnotto et al., 2010]. The concept of GND calculation was first introduced by Nye, 1953 and the detailed mathematical description of GND is given by Arsenlis and Park, 1999. In the current study an in-house python code was written based on the equations in Pantleon 2005 and 2008, Arsenlis and Park 1999 to calculate GND density and plot

slip trace map following the equations in Dunne et al., 2007. The detailed GND and slip trace calculations can be found in Biroscia et al., 2014.

3. Results and Discussion

3.1 Characterisation of the Original Material

The Waspaloy used in the current study has a relatively large γ grain size with an average size of $60 \pm 10 \mu\text{m}$ in diameter, excluding twin boundaries in the grain size calculations, see Figure 1. Moreover, the high carbon content in the alloy, see Table 1, was responsible for decorating the grain boundaries with Cr_{23}C_6 carbide precipitates that can restrict the dislocation movement during loading which further strengthen the alloy. The backscatter SEM image in Figure 1a, shows bright Cr_{23}C_6 high concentration on the grain boundaries in Waspaloy with a high magnified image in Figure 1b. It should be noticed that MC carbides, mainly $\text{Ti}(\text{Mo})\text{C}$, were also present, as indicated in the same Figures. The super EDX system in TEM was employed for carbide composition verification. Figure 2 shows that the large size of carbide on the grain boundary in Waspaloy were in fact Cr_{23}C_6 type carbide. Further TEM EDX line scan quantitative analyses were conducted for the phase verification purposes. As expected, Cr, Mo and Co mainly partitioned to the γ matrix, whilst Ti and Al are partitioned in γ' with much higher Ni content in γ' , see Figure 2. It is well established in literature that γ grain size, carbide volume fraction, secondary and tertiary γ' size and shape and the γ/γ' misfit can affect the dislocation creep mechanism to a great extent. Thus, the objective for the current study is not to compare creep performance between Waspaloy and other superalloys but rather to identify the GND accumulation in different oriented grains and their distribution effects on creep deformation mechanisms. This ultimately assisted in demonstrating the effect of GND density on failure mechanisms under different creep testing conditions. However, the effect of the grain size and carbide on GND density will be discussed in the following sections.

Figure 3 shows the EBSD-HKL derived band contrast map in (a) and Inverse Pole Figure (IPF) // Loading Direction (LD) in (b) for the as received material, i.e., prior to creep testing. As reported in Section 2.2.2 the loading direction (LD) is aligned with the normal direction (ND), i.e, orthogonal to the plane of the sample. It is clear from the figure that the original material consists of very large grains of the order of 60 μm in diameter and a relatively large area fraction of $\Sigma 3$ twin boundaries in a relatively small scanned area. It appears that the original material was not textured and contained large grains with different orientations aligned with various crystallographic fibre textures including; $<111> // \text{X-axis}$, $<100> // \text{X-axis}$ and $<110> // \text{X-axis}$. It is also evident from Figure 3c, that the as received material was fully recrystallised as the local misorientation value was very low, i.e. in an unstrained state. This is clearly reflected in the GND map, Figure 3d, which contains the same scan area as shown in Figure 3a. The average calculated GND density value was $10^{14.3} \text{ m/m}^3$. As expected, due to strain and stress incompatibilities between different oriented grains, the GND density was slightly higher in the vicinity of grain boundaries, $\sim 10^{14.8} \text{ m/m}^3$.

3.2 Waspaloy Creep Performance below Yield Stress

This minimum strain state exhibited in the as received material has subsequently changed after 500 MPa / 700°C creep loading. The EBSD band contrast map in Figure 4a shows a visible strain contouring and subgrain formation in the vicinity of the grain boundaries. Although the main fibre texture and texture components remained unchanged after the creep test, as shown in Figure 4b, the orientation gradient, i.e. orientation spread, is considerably increased within individual oriented grains. Some of the subgrains formed and local lattice rotations are indicated in Figure 4a and 4b by red arrows.

Using EBSD raw data, further quantitative analyses were performed on the sample crept at 500 MPa. The EBSD-HKL derived macroscopic $\{111\} <1-10>$ Schmid factor map is shown in Figure 4c, considering a global stress state along the loading direction (LD). Soft grains; near Cube $\{100\} <001>$

and near Goss $\{110\} <001>$ oriented grains; along with $<100> // X$ fibre texture, have a high Schmid Factor (SF), see G3 (0.4 SF), G5 (0.42 SF) with the highest value of 0.49 SF in the EBSD scanned area. Individual (111) slip traces are plotted for each grain in Figure 4d and shown in Table 2. The slip trace map and Table 2 indicate that there are at least 2 (111) slip systems that can be easily activated in the soft grains and only one slip system among the 4 (111) has a very low SF value, see G3 and G5 in Table 2. The hard grains however; near Brass $\{110\} <112>$ and near Copper $\{112\} <111>$ oriented grains on $<111> // X$ fibre texture, have lower Schmid factor values, see G1 (0.23 SF), G4 (0.24 SF), G6 and G8 (0.25 SF). It appears from the trace map in Figure 4d and Table 2, that at least 2 of the (111) slip systems have very low SF values and only one (111) slip system has a relatively high SF value. This was responsible for lowering overall SF values in the hard grains and subsequently there was not easy activation of the octahedral $\{111\} <1-10>$ slip system during creep loading. It should be noted here that the loading direction of out-of-the-plane (normal) direction (LD in Figure 4c) and the only octahedral slip system $\{111\} <1-10>$ was used for the Schmid Factor calculations. Furthermore, the hard and soft grains have different responses to creep loading, resulting in heterogeneous strain distribution and dislocation accumulation depending on the grain orientation. This is well demonstrated in the local misorientation map in Figure 4e and calculated GND map in Figure 4f. It is clear from the figures that the soft grains are less strained and contained a relatively low GND density, e.g., $10^{14.4}$ m/m³ in G3. Moreover, the hard grains showed higher local misorientation and GND density, e.g., $10^{15.3}$ and $10^{15.5}$ m/m³ in G4 and G7, respectively. This is consistent with the previous study on RR1000 during thermomechanical fatigue testing [Birosca et al., 2014]. As postulated in [Birosca et al., 2014] and demonstrated and validated here the octahedral slip system in soft grains can easily be activated (due to a high SF) and this facilitates uniform pure shear conditions and an easy yield for the soft grains without the need for grain reorientation or local element “domain” rotation. The rotation (reorientation) of a grain, i.e., slip plane, is only necessary to activate a slip system to accommodate imposed plastic deformation and generated strain during loading. Thus, this is unlikely to occur in soft grains as there are at least two (111) slip systems that can easily be activated as demonstrated in Figure 4d. Moreover, the pure shear condition in soft grains

allows unrestricted movement of dislocations on the highest SF slip system (red slip in Figure 4d) from the centre of the soft grain to the grain boundaries. This resulted in very low and relatively high GND accumulation in the centre and near the grain boundary of the soft grains, respectively. In hard grains however, i.e., not favourably oriented for octahedral slip system activation (low SF), the grain tends to rotate to activate any of the available slip systems. This causes dislocation generation “both SSD and GND” on different slip planes. Eventually, the hard grains resist the crystal rotation by accommodating further GNDs, thus causing strain hardening of the material. This leads to a high GND density on primary and secondary slip planes within the centre of the hard grains, see G1, G2, G4, G7 in Figure 4. It should be emphasized here, that the neighbouring grain orientation effect on GND location and density is reported in [Biroscia et al., 2014] and will be discussed further in the next sections. Furthermore, the small size hard grains such as G7, contain much higher GND density than the large size hard grains, e.g., G1. This is also observed by Ashby 1970. The authors of this study believe that the microstructural unit size that controls (restricts) dislocation movement can play a critical role in high GND accumulation in the small hard grains. In larger hard grains however, more free movement and wider dislocation spacing is permitted, leading to further reduction of GND accumulation. It is also reasonable to assume that this unit size factor can transform some SSD type dislocations to GND type in small grains due to size restriction, to further accommodate heterogeneous plastic strain within a limited volume. Work done by Jiang et al., 2013 shows that the average GND density does indeed vary with the grain diameter due to grain boundary hardening, but only at small strain conditions. These particular aspects and possible mechanisms of SSD/GND transformation are previously discussed by Ashby 1970, Jiang et al, 2013 and more recently by Zhu et al., 2018.

3.3 Waspaloy Creep Performance above Yield Stress

Heterogeneous plastic deformation was also found in the 800 MPa/700°C sample (anticipated to be above the material yield stress at this temperature), see Figure 5a-f. However, as shown in 5a, the

Diffraction Pattern (DP) quality was lower in 800 MPa sample which indicates higher strained conditions and is further reflected in local misorientation and GND maps in Figures 5e and 5f. The soft and hard grain correlations with GND, and strain accumulations arguments reported in the 500 MPa creep test, are consistent with that observed in the current test above yield stress. For instance, the G1, G5 ($<100>$ // X-axis) soft grains have high SF and low GND and local misorientation values, whereas G2, G3 and G4 ($<111>$ //X-axis) hard grains have low SF values with relatively high GNDs and strain accumulation, see Figure 5b-f and Table 3. The average GND density in soft grains was calculated to be $10^{14.4}$ and $10^{14.9}$ m/m³ in G1 and G5, respectively. However, the average GND density in the hard grains was $10^{15.6}$ and $10^{15.3}$ m/m³ in G3 and G4, respectively. This led to a conclusion that the average GND density value comparison between 500 MPa and 800 MPa samples does not provide a meaningful comparison, as the GND density largely depends on the grain orientations. Therefore, as the number of hard and soft grains varies depending on EBSD AOI scan area, the average GND values can change considerably in different locations of the same sample. This is in addition to the grain size effects on total GND density as discussed in Section 3.2. Furthermore, the total dislocation density value in a grain is the sum of GNDs and SSDs and work hardening of the material is controlled by both SSDs and GNDs depending on the deformation degree. Therefore, the average GND values of the samples calculated by EBSD here and in other studies does not represent overall strain accumulation and strain hardening within the materials. However, the authors of this study believe that high GND location is more indicative of their influence on strain hardening rather than their values.

It is clear that in the soft grains, two or more of the octahedral (111) slip systems could be easily activated (high SF) with only one of the (111) slip system among the 4 slips has a very low SF value in the 800 MPa/700°C crept sample, see G1 and G5 in Figure 5d and Table 3. Conversely, in the hard grains at least 3 of the octahedral (111) slip systems have very low SF values with only one slip has a relatively high SF, see G2, G3 and G4 in Figure 5d and Table 3. This is therefore consistent with the observations found in 500 MPa/700°C sample, see Figure 4 and Section 3.2. Moreover, no

preferential slip system activation among the 4 (111) octahedral slips were found in the current study. For instance, the highest SH value in G2, G3 and G4 was for (111), (1-11) and (-111) slip system in no particular order.

3.4 Transmission Kikuchi Diffraction (TKD) Characterisations

For greater insight into grain orientation correlation with slip system activation and GND density a TKD scan was performed on the 800 MPa/700°C sample. TKD allowed for much higher spatial resolution than can be achieved in a standard EBSD system. However, TKD can increase the noise floor that can affect GND calculation and obtained misorientation data. Thus, several filters have been applied to exclude any data points with misorientation angle below the angular resolution of 0.2° in addition to standard data cleaning procedures. A detailed explanation of the methods used to obtain the noise floor and angular resolution can be found in Wright, 1993 and Wilkinson and Randman, 2010. Figure 6 shows a successful TKD scan on only 3 differently oriented grains at very high resolution. Although, an ideal soft grain could not be captured using this particular TEM foil, a soft grain was imaged within 15° deviation angle from the ideal <100> // X fibre, see G3 in Figure 6. Meanwhile, an ideal hard grain (G2 in Figure 6) of <111> // X fibre was perfectly captured and imaged by the TKD scan. The TKD scan parameters and setup were already reported in Section 2.2.3. As reported in [Birosca et al., 2015, Keller and Geiss, 2012, Brodusch et al., 2013], the thickness of the sample is a critical factor in determining the quality of the TKD diffraction pattern (DP). Moreover, selecting the TKD scan area is highly dependent on the distance away from the edge of the TEM foil perforation, see Figure 6a. Very sharp DPs with 100% indexing rate were only obtained between the edge of the TEM foil perforation and 7.2 microns away from perforation edge, see the DP image within that range in Figure 6a. However, the DP quality and indexing rate reduced to less than 50% beyond 7.2 microns and 0% after 8.6 microns away from TEM foil perforation edge, see the distorted and diffused diffraction pattern at 8.6 micron in the same figure. Birosca et al., 2015, reported that the sharpest DPs can be obtained where the TEM foil thickness was ~100 nm. It seems

that the thickness of TEM foil at 8.6 microns was much thicker than 100 nm in the current study. Generally, DP quality in TKD depends on the material's atomic number and density, sample thickness, microstructure, plastic strain and SEM conditions. Nevertheless, in the present study the optimum DPs were collected between 1.5 and 7.2 microns away from the edge of the perforation, in Waspaloy using 25 kV electron beam energy. From Figure 6a, it was evident that the thickness of the TEM sample plays an important role in determining the quality of the diffraction patterns, and hence the spatial resolution and resulting orientation measurements. The effect of specimen thickness on generating transmission Kikuchi patterns is further reported in [Rice et al., 2014, Trimby 2013].

As shown in Figure 6b-e and Table 4, the conclusions reached from Figures 4 and 5 can be validated using a high spatial resolution TKD scan on 800 MPa/700°C sample. It is evident from Figure 6 that near soft grain G3 ($<100> // X\text{-axis}$) (Figure 6b) has a high SF (Figure 6c), low local misorientation (Figure 6d) and low GND (Figure 6e) values, while the hard grain G2 ($<111> // X\text{-axis}$) has low SF value with relatively higher GND and strain accumulation, see also Table 4. The GND density in G3 (soft grain) and G2 (hard grain) were measured to be $10^{14.3} \text{ m/m}^3$ and $10^{15.4} \text{ m/m}^3$, respectively. It is clear from Table 4 and {111} slip traces superimposed on IPF // LD map in Figure 6c that 3 of (111) octahedral slips have high SF values in G3 (soft grain), while 3 of the (111) slips have very low SF values in G2 (hard grain). It seems that all 4 {111} slips are not favourably oriented for activation in G2, thus the grain reoriented in order to activate any of the slip systems to accommodate the imposed plastic strain. Although (1-11) and (-111) slips have highest SF values (0.34 and 0.29, respectively), the high GND densities were observed along (11-1) and (111) slip traces, which have the lowest SF values (0.19 and 0.11, respectively), see Table 4 and black and yellow slip lines on GND map in Figure 6e. This is not surprising as the hard grain would activate any of the available slip systems non-preferentially during loading. For instance, it seems that rotating (1-11) and (-111), which have highest SF, is difficult due to the neighbouring hard grain (G1), see Figure 6c and SF values in Table 4. Thus, in order to accommodate the large plastic strain, it may be geometrically and energetically easier for (11-1) and (111) slips to be activated, since they have relatively lower SF among the 4

$\{111\}$ slips. Furthermore, due to the restriction brought about by neighbouring the top hard grain, i.e., G1 in Figure 6, the G2 grain formed large subgrains as represented in a significant orientation gradient, especially near the G1/G2 grain boundary (Figure 6c), high misorientation (Figure 6d) and GND (Figure 6e) values which eventually led to grain fragmentation of the G2 hard grain. This type of slip rotation was noteworthy and further investigated using HR-EBSD for better understanding of GND accumulation on different $\{111\}$ slip lines and the effect of neighbouring grain orientation on GND density.

3.5 HR-EBSD Observation and Cross Correlation GND Measurement

As described in Section 2.2.4, HR-EBSD was conducted for a better understanding of the grain rotation under 800 MPa/700°C creep loading condition. The HR-EBSD scan was performed on the area indicated by a dashed red rectangular shape in Figure 5a and shown in Figure 7a. The Cross Correlation based method was utilised to calculate GND density in order to obtain greater detail about dislocation density and high GND locations within a grain, see Figure 7b. Figure 7c is a magnified area in Figure 5b, showing IPF // LD for the same area in 7a. Figure 7d is a magnified GND map in Figure 5f indicated by red rectangular shape. It is clear that the GND map obtained using standard EBSD conditions with Hough Transformation parameters for GND calculations in Figure 7d and via HR-EBSD condition with applying cross correlation based method for GND calculation in Figure 7b, are very similar with greater detail in the latter.

Figure 7 shows a relatively soft grain (G1) surrounded by hard grains on the left and right hand sides (G2, G4, respectively) and below the grain (G6 and G7) as well as soft grains on the top and right bottom of the grain (G3 and G5), see Figures 7a and 7c. The GND density in the centre of the soft grain (G1) is low and very high near the grain boundaries, see Figures 7b and 7d. However, the large width of high GND density of $> 10^{15.3} \text{ m}^{-2}$ width, indicated on Figure 7d by red arrows, is in between soft and hard grains, see G1/G2, G1/G4, G1/G6, G1/G7 boundaries. However, a narrow width of high

GND density, i.e. $> 10^{15.3} \text{ m}^{-2}$, is observed between soft grain (G1) and the neighbouring soft grains (G3, G5). As discussed in Section 3.3, during the creep test, dislocations generate and move easily in the centre of soft grain G1 as the grain has high SF value and provide pure shear on at least two of the 4 (111) slips until they reach the grain boundaries. Thus, the centre of the soft grain usually shows low GND values, see Figures 7b and 7d. The SF values for three areas in G1 namely; A1, A2 and A3 as well as (111) slip traces for G1-G8 are shown in Figure 7a with data given in Table 5. From the figure and Table 5, it is evident that (1-11) slip is activated in the centre of G1 with highest SF value of 0.49 (red slip on the figure). (11-1) slip also has a high SF value of 0.46 (blue slip trace) that can be easily activated providing extra path for dislocation movement from the centre under constant loading. However, it appears that dislocation entanglement and GND accumulation near the grain boundaries depends on the neighbouring grain orientation. For instance, moving dislocations toward hard grains, i.e., G2 and G4, the slip transfer difficulty between hard and soft grain (G1/G2 and G1/G4) led to significant GND accumulation in the vicinity of the grain boundaries and constraining the grain to rotate and activate any other (111) slips. This local grain rotation in domains A2 and A3 resulted in reducing SF values of (1-11) to the lowest values of 0.07 and 0.15, respectively, and facilitates activation of (111) and (-111) instead (highest SFs in A2 and A3), see SF values in A1-A3 in Figure 7a and Table 5. This eventually resulted in lattice rotation and subgrain formation along $\langle 111 \rangle // X$ and $\langle 110 \rangle // X$ fibres in crystallographic domains of A2 and A3, respectively, as clearly demonstrated in Figure 7c. The resistance from hard grains (G2, G4) to slip transfer and domain rotation within the crystal near the grain boundaries (G1/G2, G1/G4) results in wide high-GND density areas (A2 and A3), leading to subgrain formation with large orientation deviation from the centre of the grain (A1). It seems that during constant creep loading at 700°C, the continuous movement of GNDs toward the hard grains resulted in a large width of high GND density of the order of 6.3 μm on G1/G2 grain boundary and 6.6 μm on G1/G4 grain boundary as indicated in Figure 7d. However, due to easy slip transfer and dislocation movement between the soft grains, i.e., G1 to G5 and G1 to G3, there is much less GND accumulation near soft/soft grain boundaries. This resulted in a narrow width of high-GND density of $> 1 \mu\text{m}$ on G1/G5 and G1/G3 grain boundaries. Furthermore,

as described in Biroška et al., 2014, and validated in the current study, the neighbouring grain orientation of a soft grain is the major influencing factor in GND accumulation near the grain boundary, whereas the orientation factor is a critical parameter in hard grain deformation and fragmentation. This leads to the conclusion that neighbouring grain orientation is playing a significant role in GND accumulation within the soft grains. However, the hard grains are independently constrained and eventually fragmented under their own orientation impact (low SF and high GND on multi-slips), thus neighbouring grain orientation can only assist in further constraining and accelerating the hard grain fragmentation. For further clarifications, the width of high-GND density near the hard/soft and soft/soft grain boundaries for G1 is clearly defined and visualised in HR-EBSD map in Figure 8 (indicated by black arrows) which will be further analysed in the next section.

3.6 Transmission Electron Microscopy (TEM) Investigation

As reported in Sections 2.2.1 and 2.2.2, the same TEM foil produced for TEM observation was used for EBSD and SEM characterisations. Because of the large grain size of Waspaloy and relatively small area that can be investigated in the TEM foil, it is rather straightforward to conduct TEM observation on the same EBSD map AOI. In addition to that, the cutting features on the TEM perforation edge were used as a marker for finding the area of interests (AOI)s. Here, the TEM foils used for standard EBSD and Hough transform based method for GND calculation, Figure 5, as well as HR-EBSD scan and cross correlation based method for GND measurement, Figure 7, were investigated by means of TEM, Figure 8. Figure 8 shows the GND map for an individual grain in the TEM foil for the specimen after the creep test at 800 MPa/700°C; G1 in Figure 7b. TEM images for areas A1, A2, A3, A4 and A5 as indicated on the GND map are shown in the same figure. The TEM imaging revealed the total (GND + SSD) dislocation accumulations from A1 to A5; grain centre to the grain boundary in G1. It is evident from Figure 8, that A1 and A2 (low GND density) contain low total dislocation density in the TEM image. However, both areas contain a considerable number of dislocation loops, some are indicated by dashed red oval shapes, which are considered to be the SSD

type of dislocation and cannot be measured by EBSD. Some dislocations sheared a few γ' under 800 MPa/700°C creep condition, however some γ' remained internally intact and caused Orowan dislocation looping around small size γ' , highlighted by dashed red rectangular shapes in A2. As discussed in Section 3.5, in a relatively high SF soft grain such as G1, the SSD and GND can be readily moved toward the grain boundaries, creating different GND widths depending on neighbouring grain orientation. It is clear from TEM images in A3 and A4, that the total dislocation density is increased with further approaching the grain boundaries and most of the γ' were sheared. Furthermore, it appears that most of this dislocation accumulation near the grain boundaries was owed to GND type as indicated by very high GND density in the HR-EBSD map, see A3 and A4 in Figure 8. Eventually, at the late stage of strain hardening, the total dislocation densities, and in particular the GND type, is increased dramatically when reaching the grain boundary at A5. Here, the Cr₂₃C₆ carbides on the grain boundary provided a pronounced obstacle for dislocation transfer to the neighbouring grains, that generated high GND density in A5.

A similar observation was found in the 500 MPa/700°C sample, however, much larger and multiple subgrains were formed with significantly lower dislocation intensity near the grain boundaries than in the 800 MPa/700°C sample, as shown in Figure 9a. This TEM observation is consistent with the wide ($\sim 11 \mu\text{m}$) high-GND width observed in EBSD GND map, see Figure 4f. It also appears that under 500 MPa/700°C creep test condition some of γ' were not sheared even near the grain boundary, but rather an Orowan dislocation looping was the dominating deformation mechanism, see the red square shapes in Figure 9b. Furthermore, carbides are observed to inhibit dislocation movement and slip transfer to the neighbouring grains. In general, from TEM images in Figures 8 and 9, the dislocation density near the grain boundaries in the 500 MPa sample was much less and more diffused than in the 800 MPa sample, which prevented some γ' from shearing and caused further strain hardening. This aspect will be further discussed in Section 3.7.

3.7 General Discussion

Throughout this study, it appears that subjecting Waspaloy to creep below the macroscopic yield stress would not generate dislocation (GND or SSD) in some oriented grains, but rather the imposed strain would be accommodated via rearrangement and movement of the pre-existing dislocations (GND and SSD) within those grains. It appears that the formation and movement of GNDs in the hard grains were more difficult than in the soft grains in the samples crept below yield stress. The pre-existing dislocation density in the original Waspaloy was measured to be in a range of $10^{14.4}$ - $10^{14.8}$ m/m³, see Figure 3d. These pre-existed dislocations will eventually move under creep loading, until they reach grain boundaries where they accumulate immensely, causing dislocation entanglement which depends on the microscopic stress level and creep time. It should be emphasised that the rate of dislocation mobility is largely dependent on grain orientation and availability of active slip systems. This dislocation accumulation was observed as high GND density near the grain boundaries as shown in Figure 4f and relatively high total dislocation (GND and SSD) density in the TEM observation in Figure 9. This dislocation pileup was not only observed near the grain boundaries, but also within the sub-grains, see Figures 9b and 4f. From Figure 9b, it is clear that Cr₂₃C₆ carbide on the grain boundary have contributed greatly in the dislocation accumulation and subgrain formation in the 500 MPa creep test. However, the total dislocation density and the width of high-GND density in the vicinity of the grain boundaries were lower compare to that found in the 800 MPa sample. The GND density near the grain boundaries in the 500 MPa sample was found to be $10^{15.3}$ m/m³ and a relatively large width of 11.4 μm between the hard and soft grains, see Figure 4f. This diffused high GND width has enclosed a number of large subgrains as visualised in TEM image, see Figure 9a. It appeared that the dislocation density is not very high in the 500 MPa sample compared to the 800 MPa sample, and a number of γ' were not sheared, see Figure 9b. These EBSD and TEM observations clearly indicate that the applied 500 MPa stress, i.e., below Waspaloy yield stress, was not sufficient to generate a large number of new dislocations in all oriented grains and the

movement of pre-existing SSD and GND type dislocations could not produce significant dislocation accumulation near the grain boundaries, which reflected in a large high-GND width.

Notwithstanding, it was clearly demonstrated that subjecting Waspaloy to creep above the yield stress generates new dislocations within nearly all oriented individual grains in addition to providing high mobility rate of the pre-existing dislocations. As clearly shown in the EBSD GND map and TEM images in Figures 5f and 8, respectively, the overall dislocation density in the 800 MPa sample was much higher than in the 500 MPa sample. It should be remembered that the calculated average GND values in 500 and 800 MPa samples, were $10^{15.1}$ m/m³ and $10^{15.3}$ m/m³, respectively. However, as discussed in Section 3.6, these average GND values cannot be considered representative as it is totally dependent on the numbers of hard and soft grains in the EBSD scanned area in addition to the grain size factor. Yet, the higher strained state in 800 MPa than in 500 MPa sample can be observed in the local misorientation maps in Figures 4e and 5e. As shown in Figure 8, large numbers of both SSD and GND are generated in the centre of the grain, and as in the 500 MPa sample, they move under applied stress toward the grain boundaries. These dislocations were finally entangled and appeared as high dislocation density in TEM, see Figure 8, and as GND in the EBSD map, see Figure 5f. This is well described by Gao and Huang, 1999 by a continuous movement and gliding of some dislocations in order to relax the stress (SSD), and other dislocations aligning themselves to accommodate the lattice curvature (GND). However, because of the continuous dislocation generation under 800 MPa, more intense GND and less diffused high-GND width are apparent in the 800 MPa sample. Figure 5f shows the GND density near the grain boundary in the 800 MPa sample was found to be $10^{15.5}$ m/m³ and a relatively narrow width of 6.3 μ m between the hard and soft grains, see Figure 5f. As demonstrated in Figure 8, the dislocations could shear most of the γ' near the grain boundaries. It appears that some SSD dislocations were generated in the centre and transformed to GND type near the grain boundaries. This causes a significant geometrical effect on local domain rotation and subgrain formation as was shown in Figures 5-8. This explains why most of SSD type, including dislocation loops, observed in the centre of the grain, and vast majority of the dislocations

near the grain boundary were GND type. This also explains the higher strain hardening in the 800 MPa sample compared with in the 500 MPa sample which is in an agreement with Sun et al., 2000. They showed that the lattice curvature observed in the vicinity of interfaces and the GND accumulations at grain boundary was dependent on the strain level imposed on the material. It seems that the interface, i.e., grain boundary at 800 MPa may have absorbed some GND type dislocations (i.e. exhibiting sink behavior at higher strain levels) which might cause further narrowing of the high-GND width. Furthermore, the increased strain hardening observed in the 800MPa sample (above yield) compared to the 500MPa sample (below yield) is consistent with the observation found using the Wilshire equations, that the rate of strain hardening of the material impacts on the difference found in the apparent activation energy. In the current material, above yield behaviour was characterised by an apparent activation energy (Q_c^*) of 400kJ/mol, whereas this drops to 340kJ/mol below the bulk yield stress. The findings of this work further strengthen the relationship between the lifing approach of the Wilshire equations and the micromechanical behaviour of the material in question. It appears that GND density variations in differently oriented grains, as well as the GND accumulation dependency on the location within the grains, have contributed in variation of the creep activation energies at a given stress magnitudes. For instance, during creep above yield stress, the dislocation including GNDs were generated and moved under high stress condition in almost all oriented grains. Whereas, during creep below yield stress, the new GND were only generated in some grains depending on the grain orientation. From statistical analyses it was found that no new GND was formed in most of the hard grains in the samples crept below the yield point of Waspaloy.

In summary, it is established that continuous formation of new SSD and GND dislocations in most of the oriented grains in the 800 MPa sample provided high strain hardening of Waspaloy which is in an agreement with Ashby, 1970. It was also evident that in the 800 MPa sample, the high GND density near the grain boundaries acted as a strong barrier to newly formed SSD type movement, which causes an increase in strain hardening. However, GND measurement can only give a meaningful representation of total dislocation density value if there is a large difference between

GND and SSD densities within the material. This is consistent with what Ashby, 1970 proposed, in that GND can control the work hardening of the material only if their density exceeds that of the SSD type. Hence, although SSD can be neglected in the GND measurement using both Cross Correlation and Hough Transformation based calculations, their effect however, on strain hardening cannot be ignored unless their value within the material was minimal compared to GND density value.

4. Conclusions:

It is demonstrated in the current study that although GND measurement by means of EBSD can provide a great insight of dislocation accumulation and its behaviour, it is critical to consider SSD type which also contributes to the strengthening of the materials. Thus, TEM observation is essential to have a complete description of the material strain hardening via dislocation mechanisms. This is vital to count the contributions of dislocation loops and other SSD types. In the current study, various high resolution microanalytical tools were utilised to study GND and SSD dislocation behaviour including SEM, EDS, EBSD, TKD, HR-EBSD and TEM in addition to using two methods of dislocation density for validation purposes, namely Hough Transformation and Cross Correlation based methods. The two main concepts investigated in the current study were; (i) GND accumulation in soft and hard grains and the effect of neighbouring grain orientation on local domain dislocation density, and (ii) the influence of applied stress (below and above Waspaloy yield stress) during creep on deformation mechanism and total dislocation density. Below are the main conclusions from investigating both concepts:

It was demonstrated that soft grains, i.e., high SF, provided pure shear conditions on at least two octahedral {111} slips for easy dislocation movement, reaching the grain boundary without geometrically necessary accumulation in the centre of the grain. Hence, the majority of soft grains appear to have minimum GND density in the centre of the grain with high GND accumulation in the vicinity of the grain boundaries. However, the values and width of high-GND zone depended on the

surrounding grain orientations. For instance, wide high-GND width was found between hard/soft grain boundaries whereas much narrower high-GND width was found between soft/soft grains. It was shown that this phenomenon is stress level dependent and occurred in both 500 MPa and 800 MPa samples (to a lesser extent in the former). The narrow high-GND width between soft/soft grain was believed to be attributed to easy slip and dislocation transfer between the soft grains. Conversely, the wide high-intensity GND zone widths between soft/hard grains was more attributed to strong obstacles for slip and dislocation transfer between the grains. This resulted in substantial local lattice (domain) rotation and eventually led to subgrain formation near the grain boundaries. Furthermore, it was demonstrated that hard grains, i.e., low SF grains, were not favourably oriented for any slip system activation leading to hard grain rotation in order to activate available slip systems. However, the hard grain resistance to deformation and neighbouring grain resistance for hard grain reorientation caused high GND density on a number of octahedral {111} slip systems.

It is demonstrated that during creep testing below the yield stress of Waspaloy at 500 MPa/700°C, the pre-existing GND and SSD types of dislocation move from the centre of the of the soft grain toward the grain boundaries. However, due to insufficient microscopic stress level, the GND accumulation is relatively low with a wide high-intensity GND width at the grain boundaries. In addition to the movement of pre-existing dislocations (SSD and GND) and higher mobility rate under 800 MPa/700°C creep condition, large numbers of dislocation were generated and moved toward the grain boundaries. This resulted in much higher GND density but much narrower width of high-intensity GND. It appears that the continuous generation of dislocations under 800 MPa creep stress has contributed greatly to higher strain hardening than in the 500 MPa crept sample. Moreover, it seems most of the SSD dislocation have transformed to GND type when reaching grain boundaries, causing local crystal (domain) rotation and subgrain formations. The dislocation behaviour and higher rate of strain hardening have also been linked to the increase in apparent activation energy derived from the Wilshire equations, therefore increasing confidence in the application of this creep lifing technique.

Finally, in addition to the fact that GND density largely depends on the grain orientation, the dislocation accumulation near the grain boundary depends on the neighbouring grain orientations. Thus, it is concluded that the average GND density value comparisons between 500 MPa and 800 MPa samples does not provide meaningful comparative data. This is related to the fact that the average GND values cannot be representative as they depend totally on the numbers of hard and soft grains in the EBSD scanned area in the addition to the grain size factor.

Acknowledgements

The authors would like to thank Rolls-Royce Plc for the provision of material. We also acknowledge the Rolls-Royce EPSRC Strategic Partnership (EP/H500375/1 and EP/H022309/1) for support of this work.

References:

Alexandreanu B., Sencer B., Thaveeprungsriporn V., Was G., *Acta Materialia* 51 (2003) 3831.

Arsenlis A., Parks D., *Acta Materialia* 47 (5), (1999) 1597.

Ashby M., *Philosophical Magazine* 21 (170), (1970) 399.

Birosca S., Gioacchino F., Stekovic S., Hardy M., *Acta Materialia* 74 (2014) 110.

Birosca S., Ding R., Ooi S., Coleman C., Buckingham R., Dicks K., *Ultramicroscopy* 153 (2015) 1.

Britton B., Wilkinson A., *Ultramicroscopy* 114 (2012) 82.

Brodusch N., Demers H., Gauvin R., Journal of Microscopy 250 (1), (2013) 1.

Calcagnotto M., Ponge D., Demir E., Raabe D., Materials Science and Engineering A 527 (2010) 2738.

Carter J., Kuper M., Uchi M., Mills M., Materials Science & Engineering A 605 (2014) 127.

Demir E., Raabe D., Zaafarani N., Zaefferer S., Acta Materialia 57 (2009) 559.

Di Gioacchino F., Quinta da Fonseca J. International Journal of Plasticity 74 (2015) 92.

Dunne F., Wilkinson A., Allen R., International Journal of Plasticity 23 (2007) 273.

El-Dasher B, Adams B, Rollett A. Scripta Materialia 48 (2003) 141.

Field D., Trivedia P., Wright S., Kumar M., Ultramicroscopy 103 (2005) 33.

Gao H., Huang Y., Nix W., Hutchinson J., Journal of the Mechanics and Physics of Solids 47 (1999) 1239.

Gao H., Huang Y., Scripta Materialia 48 (2003) 113.

Gourgues F., Materials Science and technology 18 (2002) 119.

Guo Y., Britton B., Wilkinson A., Acta Materialia 76 (2014) 1.

Harrison G.F. Homewood, T., Journal of Strain Analysis 29 (1994) 177.

Jiang J., Britton B., Wilkinson A., Acta Materialia 61 (2013) 7227.

Jiang J, Britton B, Wilkinson A, Ultramicroscopy 125 (2013) 1.

Jiang J., Britton B., Wilkinson A., Philosophical Magazine Letters 92 (11), (2012) 580.

Kamaya M, Wilkinson A, Titchmarsh J. Acta Materialia 54 (2006) 539.

Keller R, Geiss R., Journal of Microscopy 245 (2012) 245.

Kerr D., PhD Thesis, Resolving Geometrically Necessary Dislocations and Application in Copper, Swansea University Library, UK, 2013.

Kubin L., A. Mortensen, Scripta Materialia 48 (2003) 119.

Liu G., Salvat Canto J., Winwood S., Rhodes K., Biroscă S., Acta Materialia 148 (2018) 391.

Needleman A, Gil Sevillano J., Scripta Materialia 48 (2003) 109.

Nye J., Acta Metallurgica 1 (1953) 153.

Pantleon W., Scripta Materialia 58 (2008) 994.

Pantleon W., Materials Science and Technology 21 (12) (2005) 1392.

Pantleon W., He W., Johansson T., Gundlach C., Materials Science and Engineering A 483–484 (2008) 668.

Penkalla H., Wosik J., Czyszka-Filemonowicz A., Mater. Chem. Phys. 81 (2), (2003) 417.

Pyczak F., Devrient B., Neuner F., Mughrabi H., Acta Materialia 53 (14), (2005) 3879.

Rae C., Reed R., Acta Materialia 55 (2007) 1067.

Rice K., Kelle R., Stoykovich M., Journal of Microscopy 254 (3), (2014) 129.

Sun S., Adams B., W. E. King., Philosophical Magazine 80 (1), (2000) 9.

Trimby P., Ultramicroscopy 120 (2012) 16.

Viswanathan R., Bakker W., Journal of Materials Engineering Performance 10 (1), (2001) 81.

Whittaker M., B. Wilshire B., Metallurgical and Materials Transactions A, 44A (2013) 136.

Whittaker M., Harrison W., Deen C., Rae C., Williams S., Materials 10 (2017) 61.

Wilkinson A., Scripta Materialia 44 (2001) 2379.

Wilkinson A., Meadenb G., Dingley D., Ultramicroscopy 106 (2006) 307.

Wilkinson A., Meaden G., Dingley D. Materials Science and Technology 22 (11), (2006) 1271.

Wilkinson A., Randman D., Philosophical Magazine 90 (9) (2010) 1159.

Wosik J., Dubiel B., Kruk A., Penkalla H., Schubert F., Czyska F., Materials Characterization. 46 (2), (2001) 119.

Wright S., Journal of Computer-Assisted Microscopy 5 (3) (1993) 207.

Wright S., Field D., Materials Science and Engineering A 257 (1988) 165.

Yao Z., Zhang M., Dong J., Metallurgical and Materials Transaction. A 44 (7), (2013) 3084.

Zhu C., Harrington T., Gray III G., Vecchio K., Acta Materialia 155 (2018) 104.

Figure Captions:

Figure 1: (a) BS-SEM image of Waspaloy, (b) high magnified BS-SEM image of Cr₂₃C₆ carbide precipitation on the grain boundary and MC carbide within γ matrix.

Figure 2: TEM-EDX chemical element 2D maps confirming Cr₂₃C₆ carbide formation on the grain boundary and high titanium concentration in γ' .

Figure 3: Original Waspaloy prior to creep test (a) EBSD-HKL derived band contrast map, (b) EBSD-HKL derived IPF // LD (Z-axis) map, (c) EBSD-HKL derived local misorientation map, (d) GND 2D maps, the colour code legend is GND density values in (m^{-2}) in log scale, 100 nm step size is used.

Figure 4: Waspaloy post creep test at 500 MPa/700°C (a) EBSD-HKL derived band contrast map, (b) EBSD-HKL derived IPF // LD (Z-axis) map, (c) EBSD- HKL derived {111} <1-10> Schmid factor

map, LD = ND = Z-Axis, (d) (111) Slip Trace map; For Schmid factor values of individual planes in the map, see Table 2, (e) EBSD-HKL derived local misorientation map, (f) GND 2D maps, the colour code legened is GND density values in (m^{-2}) in log scale: 100 nm step size is used.

Figure 5: Waspaloy post creep test at 800 MPa at 700°C (a) EBSD-HKL derived band contrast map, (b) EBSD-HKL derived IPF // LD (Z-axis) map, (c) EBSD- HKL derived {111} <1-10> Schmid factor map, LD = ND = Z-Axis, (d) (111) Slip Trace map; For Schmid factor values of individual planes in the map, see Table 3, (e) EBSD-HKL derived local misorientation map, (f) GND 2D maps, the colour code legened is GND density values in (m^{-2}) in log scale: 100 nm step size is used.

Figure 6: Transmission Kikuchi Diffraction (TKD) maps of Waspaloy after creep test at 800 MPa/700 C, (a) HKL-EBSD band contrast map, (b) EBSD-derivered IPF // LD map, (c) EBSD- HKL derived {111} <1-10> Schmid factor map, LD = ND = Z-Axis; (111) slip trace map is superimposed on IPF map, for Schmid factor values of individual planes in the map, see Table 4, (d) HKL local misorientation map, (e) GND map, the colour code legened on the right is GND values in (m^{-2}) in log scale. EBSD step size of 50 nm is used.

Figure 7: HR-EBSD map for the indicated area in Figure 5a. Cross correlation method for GND calculation is applied for Waspaloy tested after creep test at 800 MPa/700°C; (a) Bruker images qualify (IQ) map (HAGB in black and LAGB in Blue), (111) slip trace map is superimposed on IQ map, for Schmid factor values of individual planes in the map, see Table 5, (b) GND map using cross correlation method for the same area in (a), the colour code legened on the right is GND values in (m^{-2}) in \log_{10} scale, e.g., $16 = 10^{16} m^{-2}$. EBSD step size of 100 nm is used. (c) magnified area of EBSD-HKL derived IPF // LD map in Figure 5b, showing standard EBSD map for the exact area in (a), (d) magnified GND map in Figure 5f for the same area in 7a.

Figure 8: GND map for an individual grain (G1 in Figure 7) for the crept sample at 800 MPa/700°C. TEM images of areas A1, A2, A3, A4 and A5, indicated on the GND map.

Figure 9: TEM images of subgrain formation on the grain boundary in the sample tested at 500 MPa/700°C. Multi subgrain formation along grain boundary in (a), (b) high magnified image of subgrain near carbide on the grain boundary.

Table Captions:

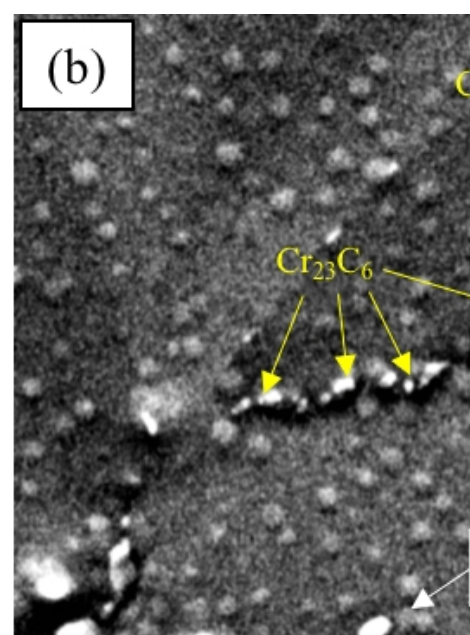
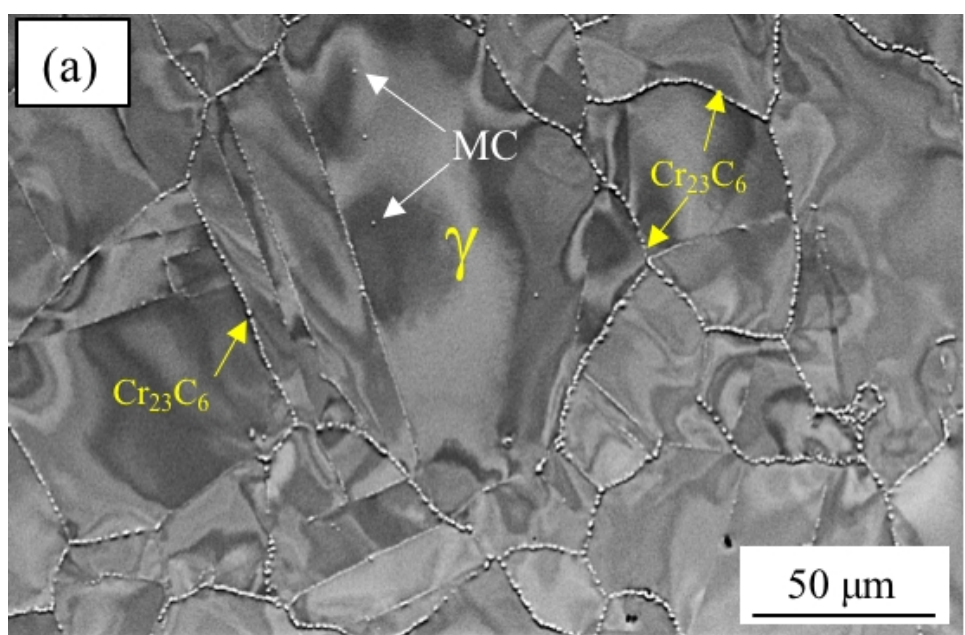
Table 1: The chemical composition of Waspaloy (wt%).

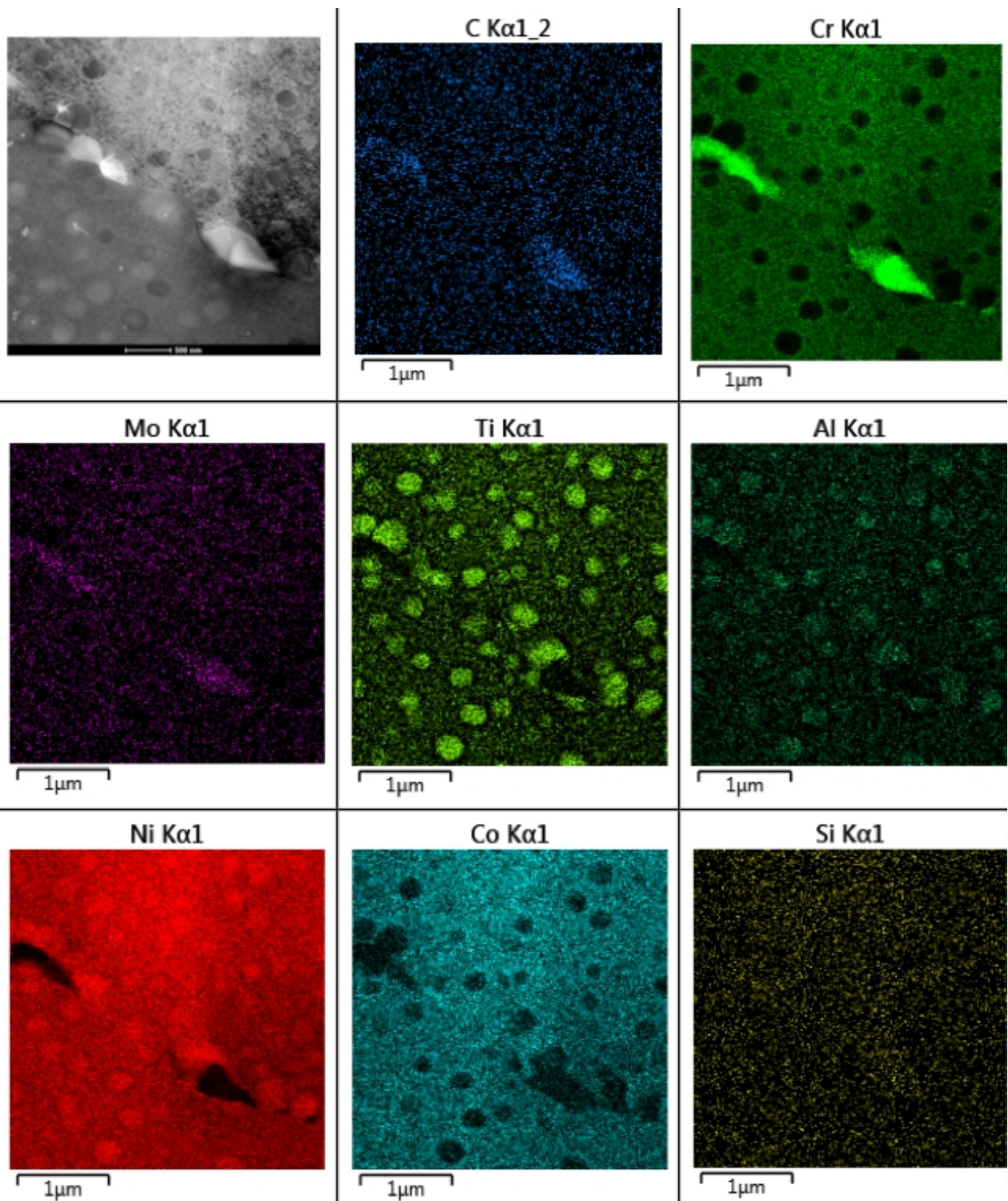
Table 2: Average and individual {111} slip system Schmid Factor (SF) values for the grains (G1-G8) indicated on Figure 4d.

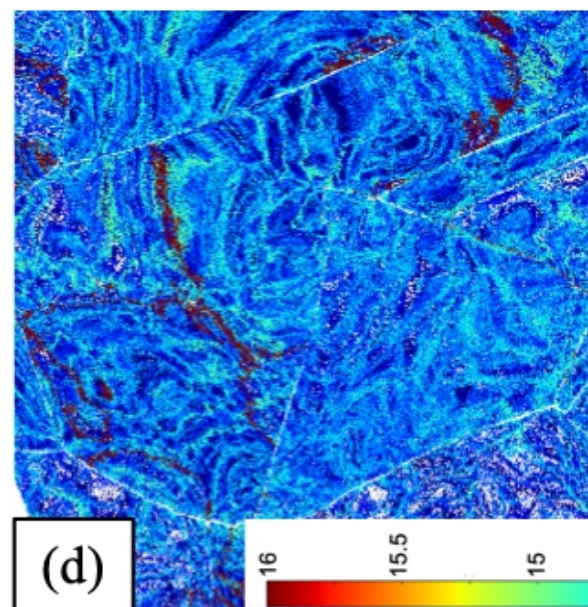
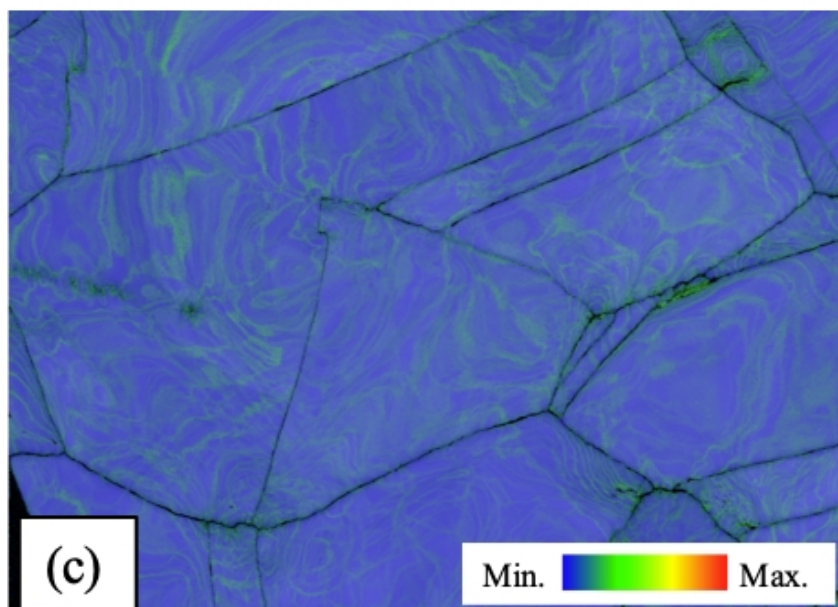
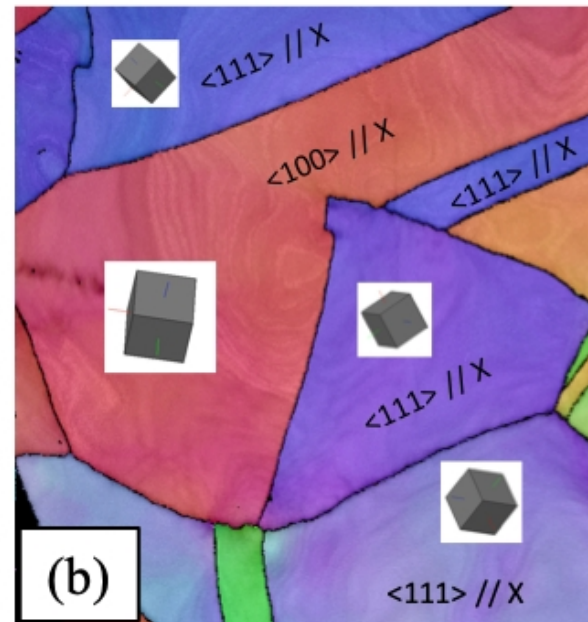
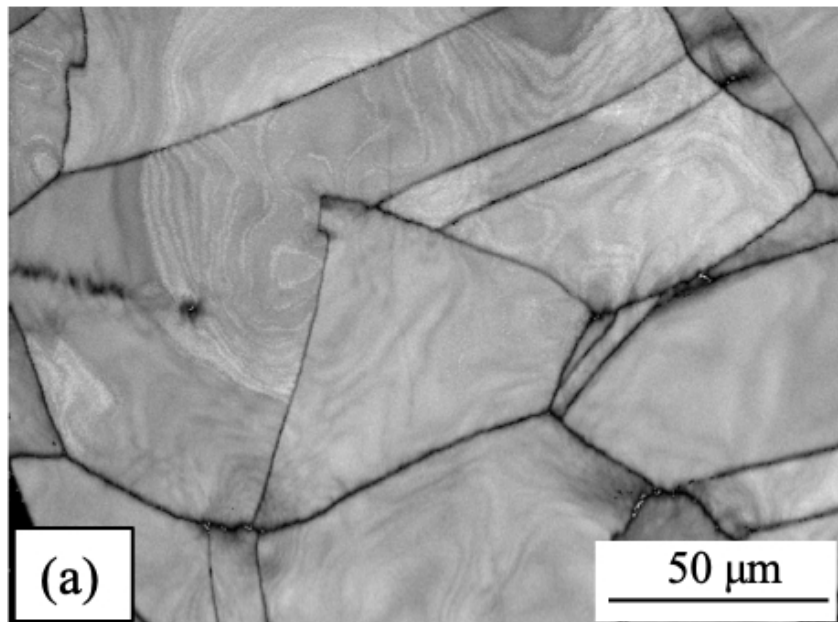
Table 3: Average and individual {111} slip system Schmid Factor (SF) values for the grains (G1-G5) indicated on Figure 5d.

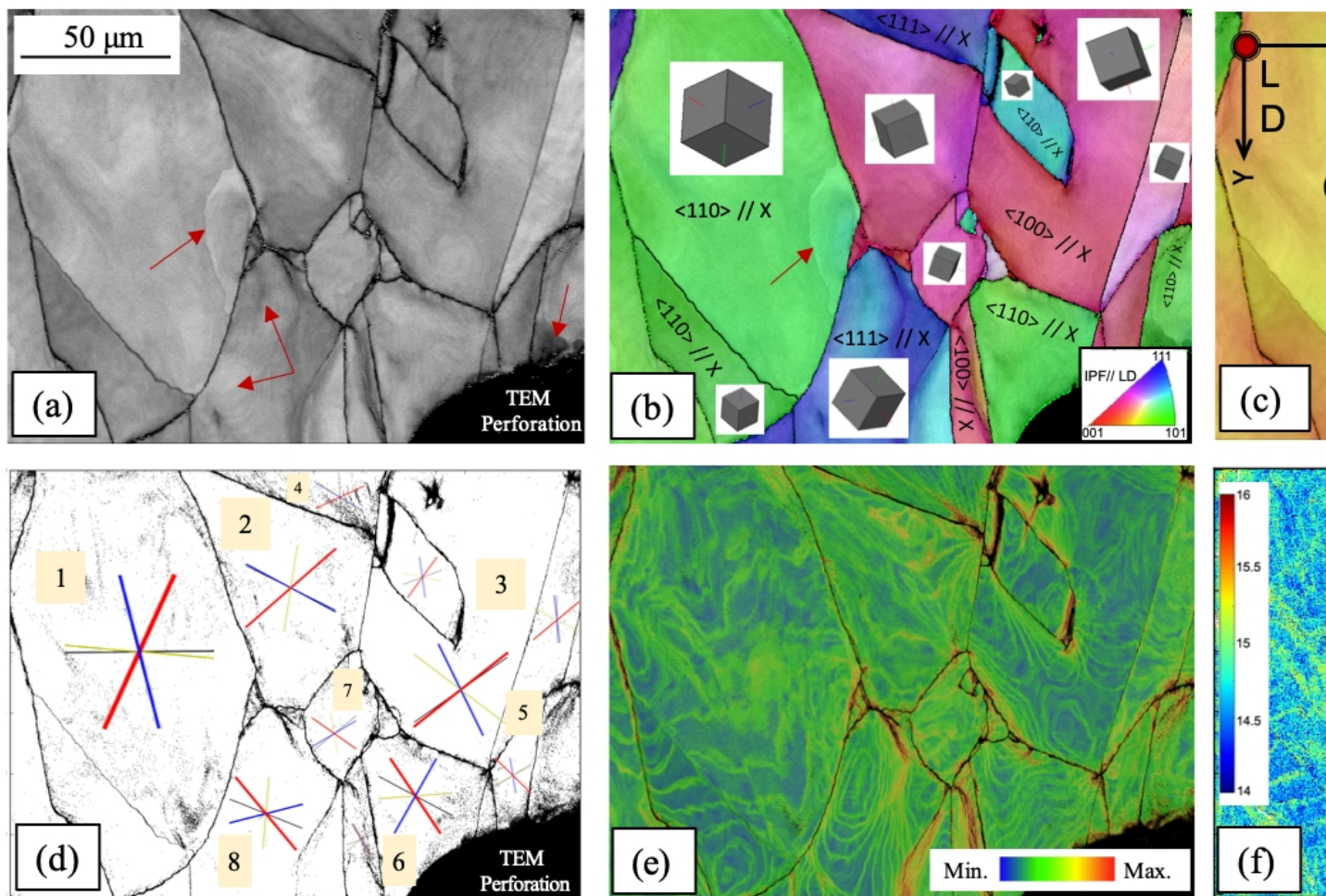
Table 4: Average and individual {111} slip system Schmid Factor (SF) values for the grains (G1, G2, G3) indicated on Figure 6b and shown in Figure 6c.

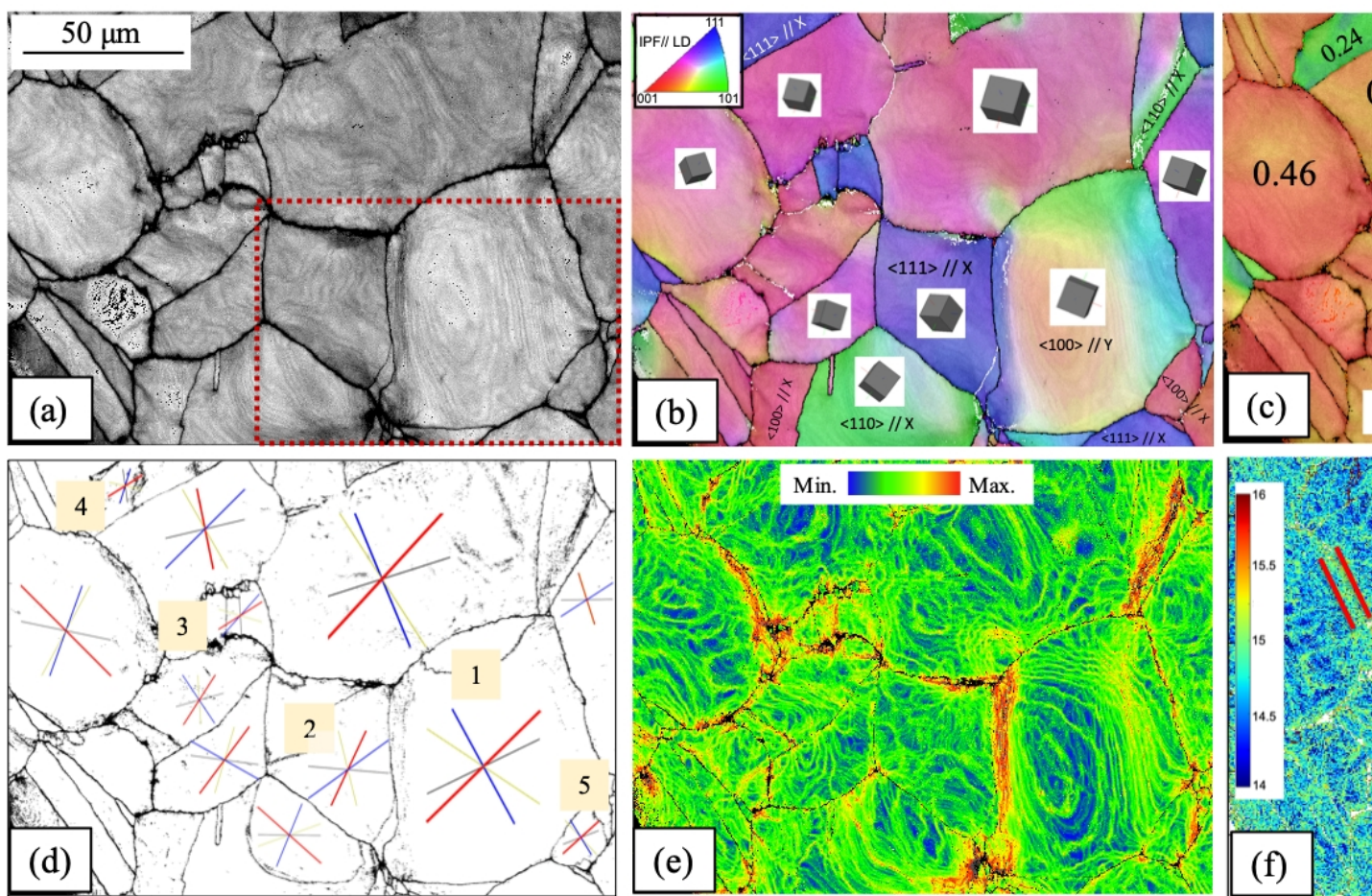
Table 5: Average and individual {111} slip system Schmid Factor (SF) values for the areas (A1, A2, A3) indicated on Figure 7a.

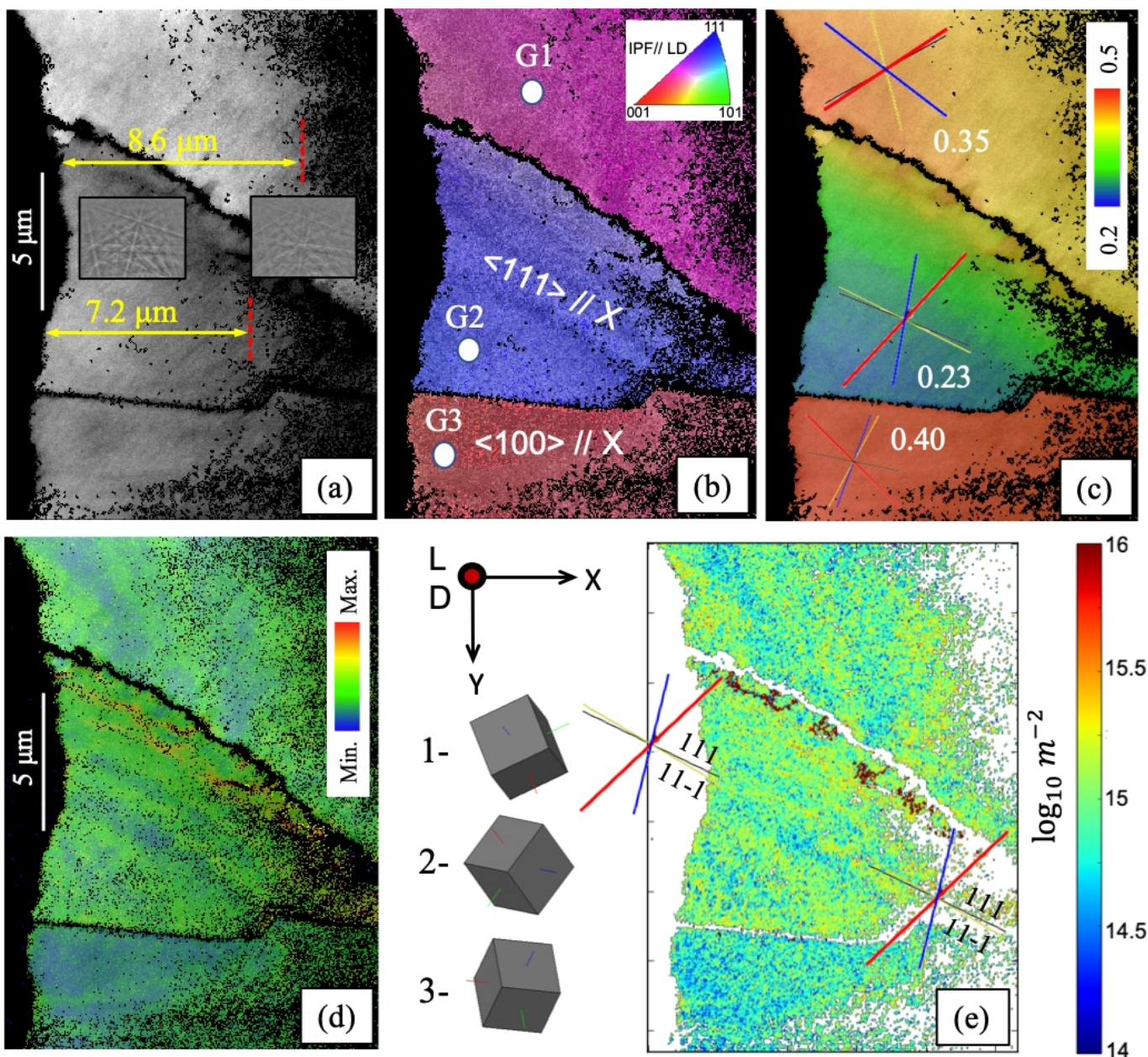


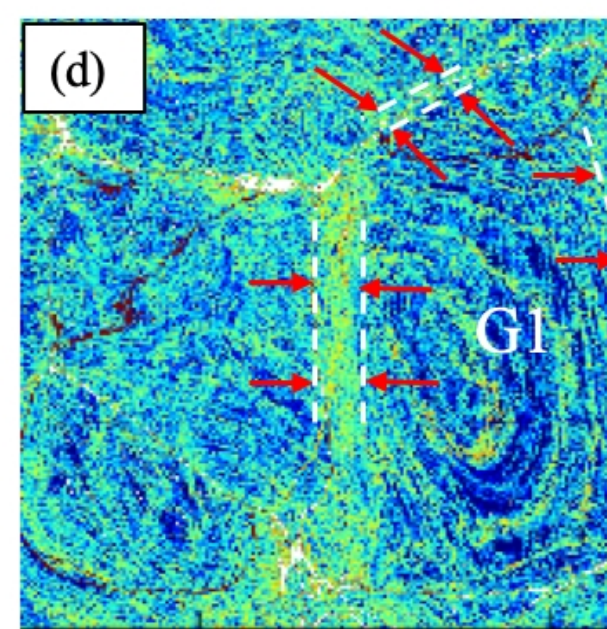
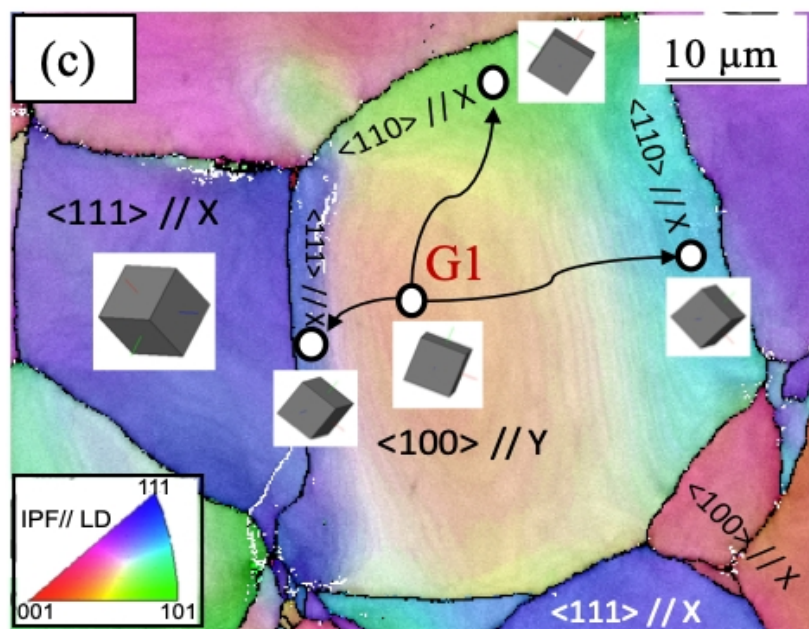
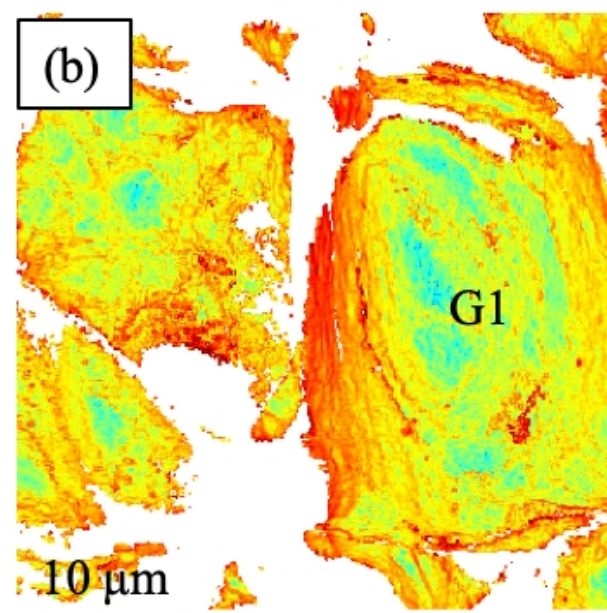
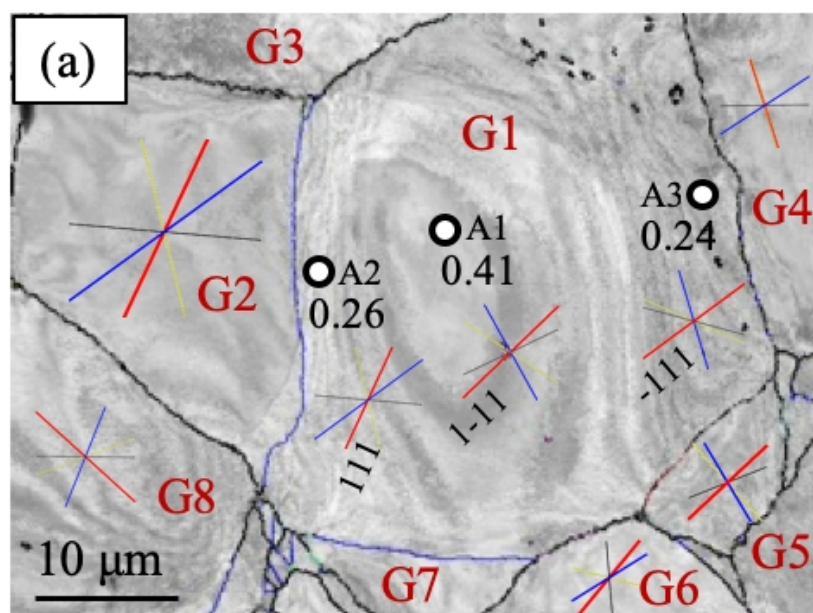


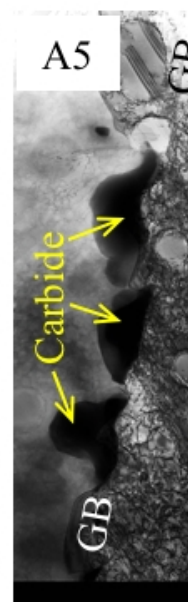
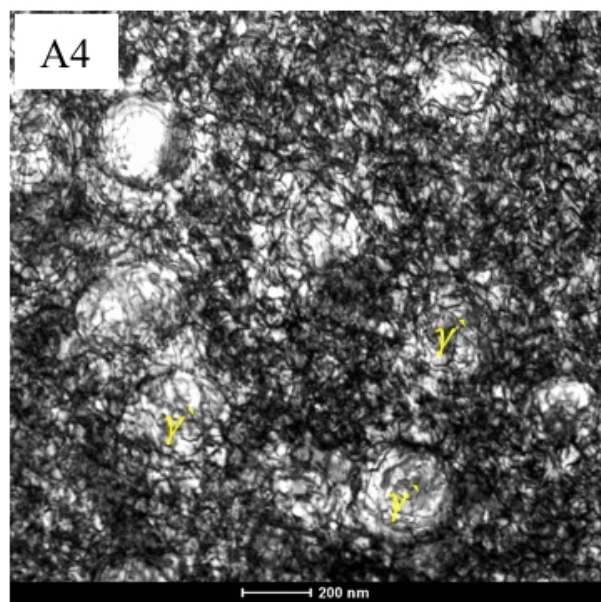
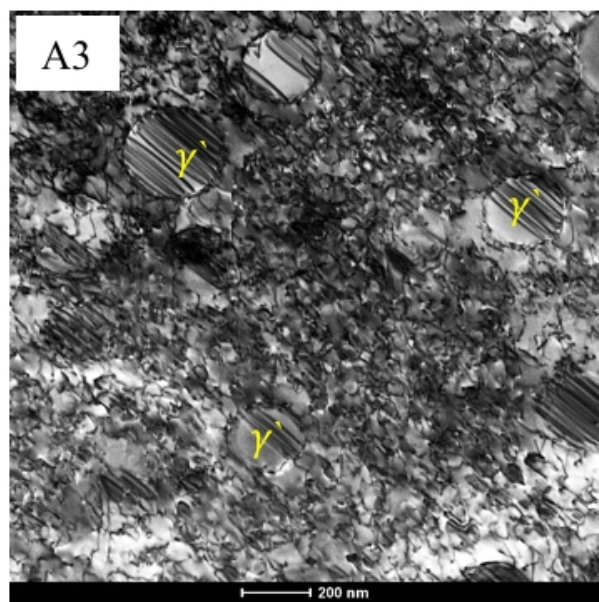
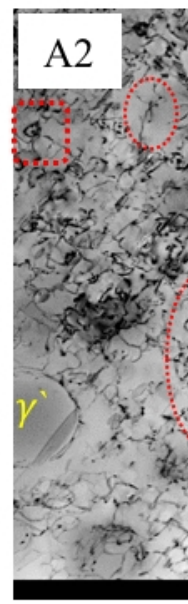
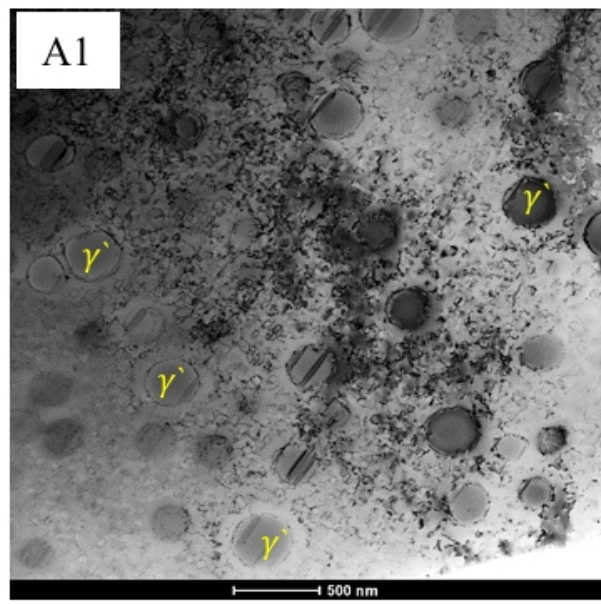
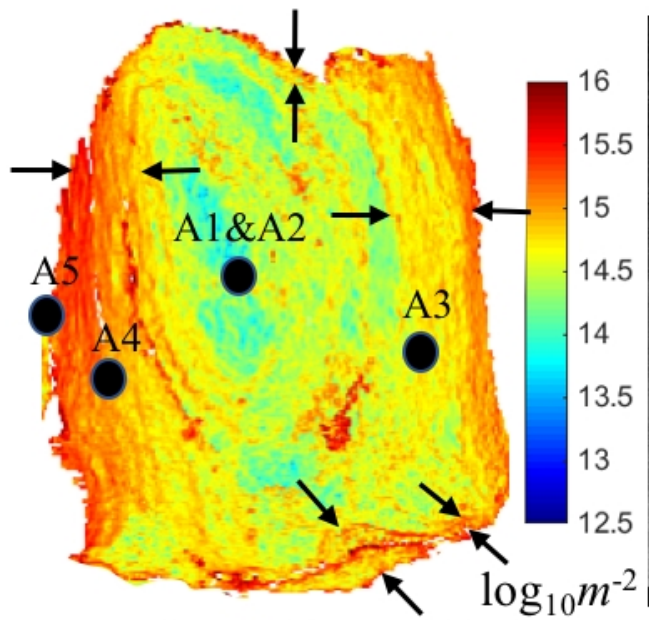


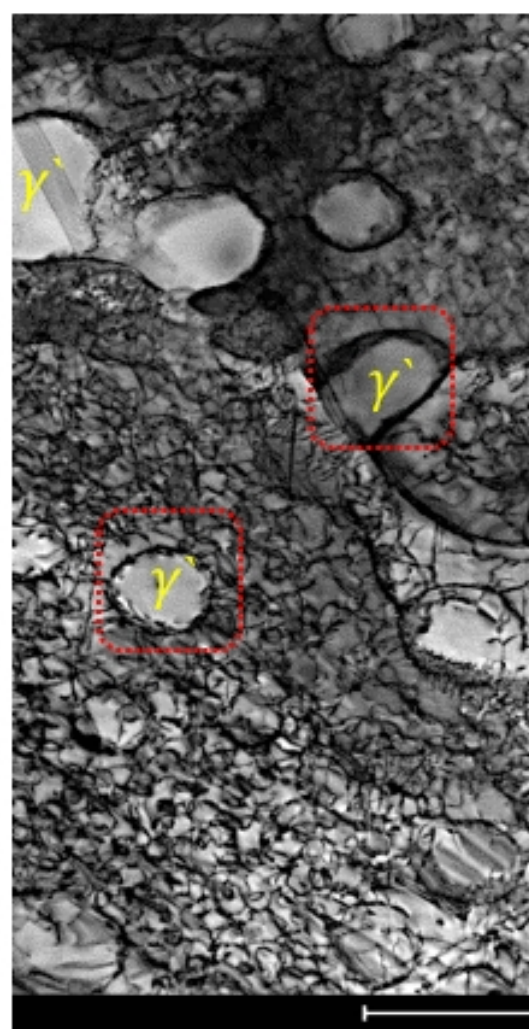
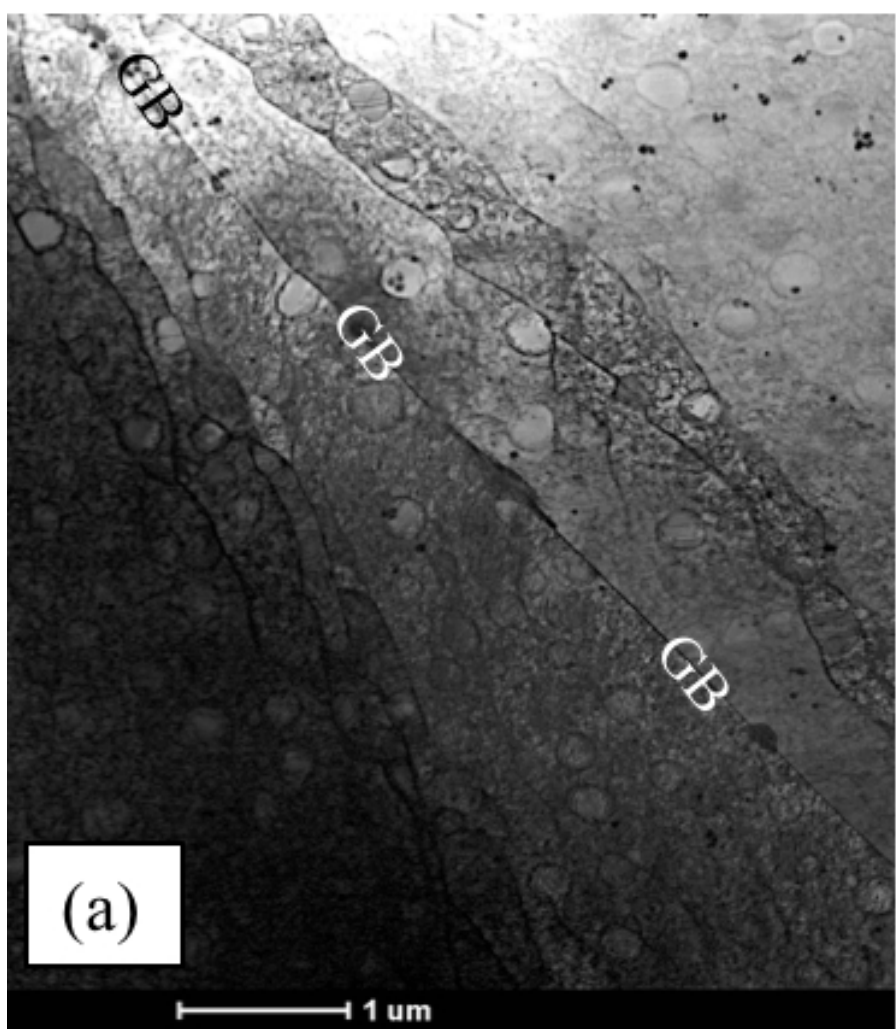












	Co	Cr	Mo	Ta	Ti	Al	C	B
Waspaloy	19.5	13.56	4.3	-	3	1.3	0.08	0.00

Schmid Factor	G1	G2	G3	G4	G5
Average	0.23	0.35	0.4	0.24	0.4
Highest	0.44	0.46	0.47	0.34	0.48
	0.40	0.41	0.44	0.34	0.44
	0.083	0.39	0.42	0.15	0.39
Lowest	0.004	0.16	0.28	0.13	0.29

Schmid Factor	G1	G2	G3	G4	G5	G6	
Average	0.41	0.26	0.21	0.18	0.14	0.12	
Highest	0.49 0.46 0.36	(11-1) (1-11) (-111)	0.40 0.33 0.25	(111) (-111) (11-1)	0.30 0.28 0.23	(-111) (111) (1-11)	0.35 0.31 0.17
	0.33	(111)	0.07	(1-11)	0.05	(11-1)	0.13
Lowest							

Schmid Factor	G1		G2	
Average	0.35		0.23	
Highest	0.47	(1-11)	0.34	(1-11)
	0.4	(11-1)	0.29	(-111)
	0.4	(-111)	0.19	(11-1)
Lowest	0.15	(111)	0.11	(111)

Schmid Factor	A1		A2		
Average	0.41		0.26		
Highest	0.49	(1-11)	0.40	(111)	0.41
	0.46	(11-1)	0.33	(-111)	0.38
	0.36	(-111)	0.25	(11-1)	0.26
	0.33	(111)	0.07	(1-11)	0.08
Lowest					